Evaporation and viscous flow structure near a contact line pinned at a solid wedge

Nikolai Kubochkin,[1] Tatiana Gambaryan-Roisman,[1] and Vladimir S. Ajaev[2]
[1]*Institute of Technical Thermodynamics, Technische Universität Darmstadt, Peter-Grünberg-Straße 10, 64287 Darmstadt, Germany*
[2]*Department of Mathematics, Southern Methodist University, Dallas, Texas 75275, USA*

(Received 14 February 2024; accepted 21 August 2024; published 23 September 2024)

Modeling of volatile droplets and rivulets on structured or rough surfaces requires detailed analysis of vapor diffusion and fluid flow near their edges where a significant amount of evaporation is expected based on both experimental data and theoretical considerations. We develop local analytical models of flow generated in these regions in both liquid and gas phases as a result of evaporation at the liquid-gas interface. Extensive parametric studies show changes in flow structure as surface wetting properties and the parameters of the surface structure/roughness are varied. Previous studies of contact lines on flat solid surfaces identified the critical contact angle above which the locally dominant flow contribution becomes independent of the evaporation rate. We find that for the contact line pinned at the wedge, this critical value increases in a nearly linear fashion as the solid wedge angle γ is decreased and develop a simple argument to explain this observation. Conditions are identified when flow separatrices can appear. The previously found separatrix emerging at contact angles slightly below the critical value persists over a range of γ but appears at higher values of the contact angle θ as γ is decreased. Increasing the gas viscosity can have a strong effect on the flow patterns in both gas and liquid. Connections between local and global solutions for several geometric configurations and implications for transport of particles in both liquid and gas phases, as well as heat transfer, are discussed.

DOI: 10.1103/PhysRevFluids.9.094007

I. INTRODUCTION

Evaporation on complex surfaces is of interest from both fundamental and practical points of view. Structured surfaces are used in ink-jet printing of electronics in order to master the deposition of conductive materials, in the production of OLED displays to achieve better precision, and are integral parts of many open microfluidic devices [1–3]. Despite the clear advantages of free-surface flows, one of the challenges in their practical applications is controlling the evaporation from the liquid-gas interface. For configurations that involve colloidal suspensions or biofluids, understanding the flows within the liquid and gas phases and their coupling during evaporation is of paramount importance for achieving the desired outcomes of particle deposition [4]. Indeed, evaporation is advantageous for drying inks and solvents but can lead to biased results in biomedical devices due to the increased concentration of solute [5]. Understanding of evaporation of liquid pinned at an edge can, in addition, enhance the comprehension of physics behind evaporation in or from porous or granular media, since an edge is the simplest element of their intricate geometries [6]. Moreover, it can help gain further understanding of the dynamics of salt solutions during efflorescence and subflorescence, since brine evaporation near the edges of freshly precipitated crystal is considered to be one of the factors promoting further crystal growth [7,8]. Salting out is, in turn, a challenge commonly faced in the development of desalinating evaporators [9].

In the following, we do not attempt to cover the entire body of literature on evaporation of sessile droplets and rivulets, as a tremendous amount of research has been carried out on the topic over the past several decades, but rather focus on the works most relevant for the developments in the present study. For obtaining a broader picture, we refer the reader to the review papers of Cazabat and Guéna [10], Erbil [11], Larson [12], Zang *et al.* [13], Wilson and D'Ambrosio [14], and Ajaev and Kabov [15].

If a liquid evaporates slowly into still air, evaporation can be considered a quasistationary process limited by the diffusion of vapor molecules. That assumption has been, for example, used in order to explain the residuals left after evaporation of a particle-laden drop on a planar rigid surface [16]. The transport of particles in evaporating droplets motivated several important studies of liquid flow inside the droplet. Tarasevich [17] obtained an analytical solution for the potential flow within a semispherical droplet. A thin-film approach was employed by Fischer [18] to obtain the flow structures within a droplet for different functional forms of evaporative mass fluxes. Hu and Larson used a thin-film theory as well as finite-element simulations to study the flow in a droplet [19], also taking into account the Marangoni effect [20], i.e., contribution to the flow due to surface tension gradients caused by nonuniform interfacial temperature. Remarkably, the direction of flow leading to accumulation of particles near the edge of the droplet can be reversed by these surface tension gradients [21,22]. Possibility of spatial variation of surface tension due to surface contamination in experiments has also been discussed [23].

When a droplet or rivulet evaporates, the contact line region—where solutes in many cases tend to agglomerate—is the area of immense interest. Therefore, local solutions are often obtained and analyzed. Whereas for evaporation into pure vapor, a well-known microregion model based on a thin-film theory [24–26] is used, the local contact line solutions for the diffusion-limited evaporation of droplets inherit the mathematical machinery developed many decades ago in several pioneering studies [27–29] of the viscous liquid flow in a sharp corner with straight walls. Moffatt [29] obtained similarity solutions for the Stokes flow in sharp corners and, importantly, was the first to recognize that the complex-valued local solutions obtained previously by Dean and Montagnon [28] correspond to a set of eddies emerging in the corner [30]. The problem of the corner flow has been addressed and generalized for the case of the curved corner walls by Voinov [31]. Special points in Stokes flow, such as points in the stagnation regions and near protruding cusped edges, were discussed in the works of Michael and O'Neill [32] and Jeffrey and Sherwood [33]. Significant advances in understanding local viscous flow solutions have been made by Gelderblom *et al.* [34,35] who employed the Stokes flow approximation for the problem of sessile droplet evaporation both on a flat rigid substrate and a liquid pool surface. They have considered three local solutions: flow induced by evaporation, flow due to liquid-gas interface motion, and an eigenmode, i.e., the solution that satisfies the homogeneous boundary conditions. Remarkably, they have shown that depending on the contact angle either an eigenmode or an evaporation-induced solution will dominate the flow structure, and obtained a critical angle of 133.4° at which the dominating contribution to flow changes (for a droplet on a flat rigid substrate). For a liquid with the contact angle smaller than the critical value, the evaporation-induced flow dominates the eigenmode solution. While Gelderblom *et al.* [34] consider contact lines on a flat surface, a problem of pinning of evaporating liquid at wedge-shaped structures is also of interest and is considered in the present work. Hong *et al.* [36] studied evaporation near a permeable wedge-shaped deposit of particles. They have discussed the mechanism of the deposit growth and performed the stability analysis of the contact line. Evaporation of droplets in rectangular grooves and cylindrical wells has been investigated by Okuzono *et al.* [37] and D'Ambrosio *et al.* [38], but no local solution structures were discussed in these studies.

In all studies described above, a single-phase model of evaporation is employed, so that no flow in the gas phase is accounted for. Importance of convective flows in the gas for sessile droplet evaporation was highlighted by, e.g., Carle *et al.* [39]. Recently, the problem of liquid evaporation near a contact line has been examined by Ajaev and Kabov [40] who considered the configuration of a circular dry patch in a liquid layer. The authors demonstrated that taking into account the so-called

Stefan flow [41,42] in the gas phase is crucial for the understanding of the liquid flow topology and can change the latter significantly. The changes in the liquid flow structure, in turn, can change the deposition patterns. The Stefan flow is also believed to play a significant role in the behavior of droplets levitating over a surface of a heated liquid [42] and can affect the trajectories of microscale droplets inhaled into human respiratory airways [43].

In the present work, we investigate the evaporation of droplets and rivulets on surfaces with protruding wedge-type features and analyze local flows in liquid and gas phases in the vicinity of the contact line pinned to those wedges. We take advantage of a Stokes flow model and take into account the Stefan flow. Thus, we generalize the solution obtained by Ajaev and Kabov [40] making it applicable for the case of arbitrary solid and liquid angles. We first describe our mathematical model and obtain analytical solutions for the evaporation-induced flow. After that, we discuss the "peculiar points" of the solution and plot a number of typical flow patterns.

II. MATHEMATICAL FORMULATION OF THE PROBLEM

A. Evaporation-induced flow

Let us consider a droplet or a rivulet of a volatile liquid in a gaseous environment on a structured, fractured, porous, or simply rough surface. The contact lines where liquid surfaces touch the solid are known to pin easily on the elements of surface topography [44] and, hence, we consider a pinned contact line hereafter. Let L be a characteristic length scale of the surface topography. When the evaporation process occurs, flow not only in the liquid but also in the gas phase has to be considered. The latter is attributed to a Stefan flow, i.e., hydrodynamic motion that occurs to compensate for lack of balance between diffusion fluxes of vapor molecules and components of dry air, as explained in more detail in [42]. The Stefan flow velocity U is used as a characteristic velocity scale of the problem and is defined below. In close proximity to the contact line, it can be assumed that liquid-gas, liquid-solid, and solid-gas interfaces are straight lines. The geometry of such a three-phase system is hence represented by three adjoining wedges (Fig. 1). The contact angle from the liquid side is θ, the wedge angle of the element of the substrate topography is γ, and the angle corresponding to the gas phase region is $\beta = 2\pi - \theta - \gamma$. The flows in the liquid (components denoted by subscript l hereafter) and gas (subscript g) are two-dimensional and, since in the immediate vicinity of the contact line the Reynolds number is expected to be vanishingly small, obey the Stokes flow equations. To take advantage of the local geometric configuration, we employ a polar coordinate system with the origin at the contact line and zero polar angle φ at the liquid-gas interface. The variable r measures the distance and φ measures the angle. Since the liquid-gas interface is represented by a straight line segment in our formulation, our solution is valid only for r which are much smaller than the radius of curvature of the interface. This condition is not particularly restrictive for macroscopic droplets but is more difficult to satisfy when the interfacial curvature is set by the size of the microstructure, i.e., when a rivulet or a microscopic droplet is trapped within the structure. For the rivulet shown in Fig. 1(b), the curvature can be expressed in terms of the distance between the contact lines a as $(2/a)\cos(\theta + \gamma/2)$. Thus, the radius of curvature is small and the requirement of r being even smaller may be difficult to satisfy, especially when the angle θ gradually decreases due to evaporation.

The radial v_r and angular v_φ velocities in liquid and gas can be written as

$$v_{r,g} = \frac{1}{r}\frac{\partial \psi_g}{\partial \varphi}, \quad v_{r,l} = \frac{1}{r}\frac{\partial \psi_l}{\partial \varphi}, \quad v_{\varphi,g} = -\frac{\partial \psi_g}{\partial r}, \quad v_{\varphi,l} = -\frac{\partial \psi_l}{\partial r}, \tag{1}$$

and satisfy biharmonic equations

$$\nabla^4 \psi_g = 0 \text{ and } \nabla^4 \psi_l = 0, \tag{2}$$

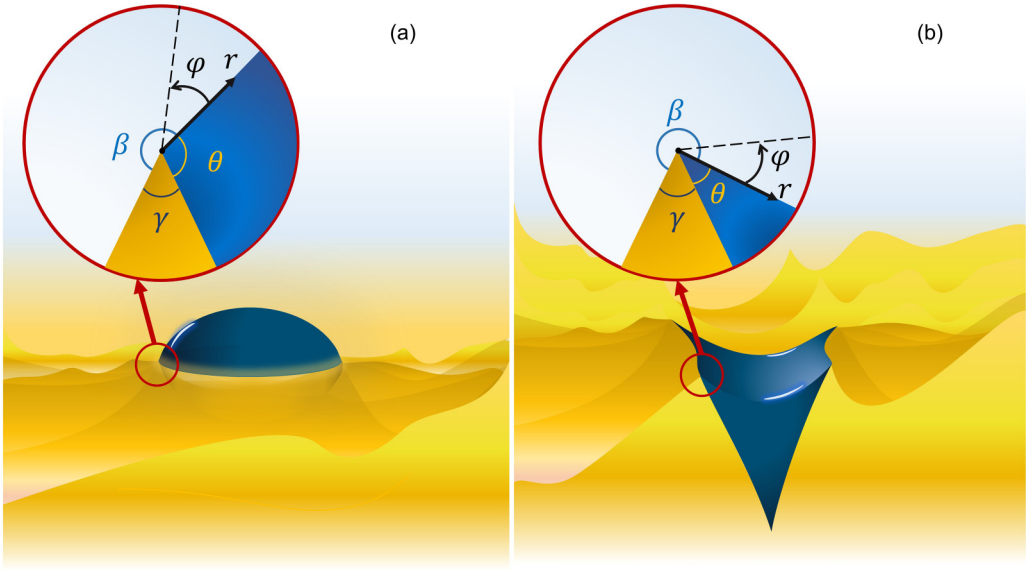

FIG. 1. Configurations of a liquid on a rough or structured surface: (a) a liquid droplet and (b) a liquid rivulet. The inset pictures show the contact line region. The angles θ, γ, and β denote contact angle of a liquid, angle of an element of the solid structure and the gas phase angle, respectively. The polar coordinate system is chosen such that the polar angle $\varphi = 0$ at the liquid-gas interface.

where ψ_g and ψ_l are the stream functions in the gas and liquid, respectively. The general solutions of (2) are superpositions of terms of the form

$$\psi_g = r^m f_{g,m}(\varphi) \text{ and } \psi_l = r^n f_{l,n}(\varphi), \tag{3}$$

where the angular functions $f(\varphi)$ for $m, n \neq 0, 1, 2$ have the following form:

$$f_{g,m}(\varphi) = A_g \cos m\varphi + B_g \sin m\varphi + C_g \cos (m-2)\varphi + D_g \sin (m-2)\varphi, \tag{4}$$

$$f_{l,n}(\varphi) = A_l \cos n\varphi + B_l \sin n\varphi + C_l \cos (n-2)\varphi + D_l \sin (n-2)\varphi. \tag{5}$$

The coefficients in (4) and (5) can be determined from the boundary conditions as follows. First, for the liquid, the no-slip condition $v_{r,l} = 0$ and no-penetration condition $v_{\varphi,l} = 0$ are imposed at the liquid-solid interface $\varphi = -\theta$. For the gas, at the solid-gas interface $\varphi = \beta$ we similarly have $v_{r,g} = 0$ and $v_{\varphi,g} = 0$. Taking into account (1) and (3), one arrives at the following conditions:

$$f_{l,n}(-\theta) = 0, \; f'_{l,n}(-\theta) = 0, \tag{6}$$

$$f_{g,m}(\beta) = 0, \; f'_{g,m}(\beta) = 0, \tag{7}$$

where prime designates a derivative with respect to φ. When crossing the liquid-gas interface, the equality of the radial components of the velocities of liquid and gas is expressed as

$$f'_{g,m}(0) = f'_{l,n}(0). \tag{8}$$

The angular velocities at the liquid-gas interface are related to the evaporative mass flux J as

$$v_{\varphi,l}(r, 0) = J\rho \text{ and } v_{\varphi,g}(r, 0) = J, \tag{9}$$

where $\rho = \frac{\rho_a}{\rho_l}$ with ρ_a and ρ_l being densities of gas (air) and liquid and the evaporative flux J being scaled by $\rho_a U$. Additionally, at the liquid-gas interface, the tangential stress balance reads

$$\mu\left[r\frac{\partial}{\partial r}\left(\frac{v_{\varphi,g}}{r}\right)+\frac{1}{r}\frac{\partial v_{r,g}}{\partial \varphi}\right]_{\varphi=0}-\left[r\frac{\partial}{\partial r}\left(\frac{v_{\varphi,l}}{r}\right)+\frac{1}{r}\frac{\partial v_{r,l}}{\partial \varphi}\right]_{\varphi=0}=0, \tag{10}$$

where $\mu = \frac{\mu_g}{\mu_l}$ with μ_g and μ_l being dynamic viscosities of the gas and liquid, respectively. For water at normal pressure and temperature of $T = 79\,^{\circ}\mathrm{C}$, corresponding to the experimental conditions discussed in [40], the liquid viscosity is $3.580 \times 10^{-4}\,\mathrm{Pa\,s}$, while the corresponding saturated moist air viscosity is $1.639 \times 10^{-5}\,\mathrm{Pa\,s}$ [45], leading to $\mu = 0.0458$. For a wide range of realistic experimental conditions, the value of μ does not exceed 0.1. In the results presented below we consider two representative cases: vanishingly small viscosity ratio, $\mu = 0$, and small but non-negligible value of $\mu = 0.1$.

We assume that the contribution of the evaporation-induced Marangoni stresses to the shear-stress balance is negligibly small. To justify this assumption, we note that the local temperature distribution in the liquid, assuming constant solid wall temperature and prescribed heat flux to maintain evaporation, suggests that the surface tension gradient behaves as r^{n-1} as $r \to 0$. However, the viscous stresses in Eq. (10) are $\sim r^{n-2}$ and therefore locally dominate the Marangoni-induced stresses.

Condition (10) can be formulated in terms of the stream functions (1) as follows:

$$\mu\left[r\frac{\partial}{\partial r}\left(\frac{1}{r}\frac{\partial \psi_g}{\partial r}\right)-\frac{1}{r^2}\frac{\partial^2 \psi_g}{\partial \varphi^2}\right]_{\varphi=0}-\left[r\frac{\partial}{\partial r}\left(\frac{1}{r}\frac{\partial \psi_l}{\partial r}\right)-\frac{1}{r^2}\frac{\partial^2 \psi_l}{\partial \varphi^2}\right]_{\varphi=0}=0. \tag{11}$$

Since the exponents in (3) and the coefficients in (4) and (5) are not yet known, we now need to have a closer look at the evaporation process to determine them. Let the vapor partial density field in the gas phase be ρ_v, while the partial density of dry air components is ρ_g. Vapor molecules can be transported away from the liquid-gas interface by diffusion and carried away by the flow in the gas phase. The effects of natural convection are typically neglected in the studies of evaporating droplets and rivulets. This approximation, also used in the present work, is justified by estimates of the relevant nondimensional numbers and by many direct comparisons between experimental data and model predictions [10,14]. However, another contribution to convective vapor transport, due to Stefan flow discussed above, is accounted for in our study. Specifically, we assume the vapor mass flux j to include diffusion, described by Fick's law, as well as the Stefan flow as follows:

$$j = -D\nabla\rho_v + U\rho_v, \tag{12}$$

where D is the diffusion coefficient for vapor molecules in moist air. Using a quasisteady approximation, to be justified below, and the fact that Stefan flow compensates for the diffusive flux of molecules of dry air, the Stefan flow velocity is $U = \frac{D_g \nabla \rho_g}{\rho_g}$. Here D_g is the diffusion coefficient of the dry air components through moist air, which we assume to be equal to D. Furthermore, if we assume that the total moist air density is constant, the ratio of the second term on the right-hand side of Eq. (12) to the total flux can be expressed as

$$\frac{\rho_v U}{j} = \frac{\rho_v(-D\nabla\rho_v)/\rho_g}{-D\nabla\rho_v - \rho_v D\nabla\rho_v/\rho_g} = \frac{\rho_v}{\rho_v + \rho_g}. \tag{13}$$

Thus, the relative importance of Stefan flow is determined by $\rho_v/(\rho_v + \rho_g)$, a ratio which is not negligibly small even for moderate heating (e.g., estimated to be 0.45 for water vapor at 85 °C). Our results suggest that the transport is dominated by diffusion only at low temperatures, close to room temperature, while increasing the temperature gradually leads to a situation similar to when the gas phase is pure vapor and thus flow, not diffusion, is the relevant transport mechanism.

Let the vapor concentration far away from the liquid-gas interface be $\rho_{v,\infty}$ and the subscript lg be referring to quantities at the liquid-gas interface. The velocity scale, set by the Stefan flow, can

be defined as $U = \frac{D(\rho_{v,lg}-\rho_{v,\infty})}{\rho_g L}$. The Péclet number $\mathrm{Pe} = \frac{LU}{D}$ is estimated be on the order of 10^{-2} or less. The concentration/density field can hence be obtained from the stationary diffusion equation

$$\nabla^2 c = 0 \tag{14}$$

written in terms of dimensionless density $c = \frac{\rho_v-\rho_{v,\infty}}{\rho_{v,lg}-\rho_{v,\infty}}$. The boundary conditions for Eq. (14) read

$$c\Big|_{\varphi=0} = 1 \text{ and } \frac{\partial c}{\partial \varphi}\Big|_{\varphi=\beta} = 0. \tag{15}$$

The solution of (14) can be written as a series in powers of r, which in the immediate vicinity of the contact line, $r \to 0$, becomes

$$c \approx 1 + r^\lambda K_\lambda \sin\lambda\varphi = 1 + r^\lambda K_\lambda \cos\lambda(\varphi-\beta) \tag{16}$$

with the exponent $\lambda = \frac{\pi}{2\beta}$. For a flat solid surface, the exponent reduces to the well-known value of $\lambda = \frac{\pi}{2(\pi-\theta)}$. The evaporative flux then reads $J = \lambda K r^{\lambda-1}$. The coefficient $K_\lambda \equiv K$ cannot be obtained from the local considerations and requires the solution of the global problem. Provided an expression for J, combining equations (1), (3), and (9), one can conclude that $\lambda = m = n$. The velocity boundary conditions (9) are rewritten for the stream functions as

$$f_{g,m}(0) = -K \text{ and } f_{l,m}(0) = -K\rho. \tag{17}$$

Finally, when relations (3) are used and (17) are accounted for, (11) reduces to

$$\mu f''_{g,m}(0) - f''_{l,m}(0) = K\lambda(\lambda-2)(\rho-\mu). \tag{18}$$

Now, as all eight boundary conditions (6), (7), (8), (17), and (18) are formulated, the coefficients of the stream functions (4) and (5) can be determined from a linear system of equations with the coefficient matrix $\mathbf{E}$:

$$\mathbf{E} = \begin{pmatrix} E_{11} & E_{12} & E_{13} & E_{14} & 0 & 0 & 0 & 0 \\ 0 & 0 & 0 & 0 & E_{25} & E_{26} & E_{27} & E_{28} \\ E_{31} & E_{32} & E_{33} & E_{34} & 0 & 0 & 0 & 0 \\ 0 & 0 & 0 & 0 & E_{45} & E_{46} & E_{47} & E_{48} \\ 1 & 0 & 1 & 0 & 0 & 0 & 0 & 0 \\ 0 & 0 & 0 & 0 & 1 & 0 & 1 & 0 \\ 0 & \lambda & 0 & \lambda-2 & 0 & -\lambda & 0 & 2-\lambda \\ \lambda^2 & 0 & (\lambda-2)^2 & 0 & -\mu\lambda^2 & 0 & -\mu(\lambda-2)^2 & 0 \end{pmatrix}, \tag{19}$$

where the matrix elements are as follows: $E_{11} = \frac{E_{32}}{\lambda} = \cos\theta\lambda$, $E_{12} = -\frac{E_{31}}{\lambda} = -\sin\theta\lambda$, $E_{13} = \frac{E_{34}}{\lambda-2} = \cos(\lambda-2)\theta$, $E_{14} = -\frac{E_{33}}{\lambda-2} = -\sin(\lambda-2)\theta$, $E_{25} = \frac{E_{46}}{\lambda} = \cos\beta\lambda$, $E_{26} = -\frac{E_{45}}{\lambda} = \sin\beta\lambda$, $E_{27} = \frac{E_{48}}{\lambda-2} = \cos(\lambda-2)\beta$, $E_{28} = -\frac{E_{47}}{\lambda-2} = \sin(\lambda-2)\beta$. Let us also define a vector $\mathbf{b}$ such that $b_5 = -\rho K$, $b_6 = -K$, $b_8 = \lambda(\lambda-2)(\rho-\mu)K$, and all other components are equal to zero. A linear system defined by the matrix from Eq. (19) and the vector $\mathbf{b}$ on the right-hand side can be solved analytically. However, since the solution turns out to be rather cumbersome, we introduce auxiliary functions as follows:

$$\mathcal{H}_\pm(\lambda, x) = (\lambda-1)\cos 2x \pm \cos 2x(\lambda-1) - \lambda, \tag{20}$$

$$\mathcal{M}_\pm(\lambda, x) = \sin 2x(\lambda-1) \pm (\lambda-1)\sin 2x, \tag{21}$$

$$\mathcal{G}(\lambda, x) = \cos 2x(\lambda-1) + (\lambda-2)\lambda - (\lambda-1)^2\cos 2x, \tag{22}$$

$$\mathcal{P}(\lambda) = (\lambda-2)(\lambda\mu - \lambda\rho + \rho) \tag{23}$$

to make it more compact. The solution for coefficients A_g, B_g, C_g, D_g, and A_l, B_l, C_l, D_l of functions ψ_g and ψ_l is presented in the Appendix.

B. Eigenmode solution

The results of the local analysis for the case of $\gamma = \pi$, i.e., flat solid substrate, presented by Gelderblom *et al.* [34], suggest that the so-called eigenmode solution can dominate the local flow for a range of contact angles. The eigenmode solution satisfies Eq. (2) with the homogeneous boundary conditions. The value of λ_e for the eigenmode solution is different from the λ obtained above for the local flow induced by evaporation because in the conditions (17) we set $K = 0$. However, m and n are still related through conditions (8) and (18) and, hence, $m = n = \lambda_e$. The stream functions can be written as

$$\psi_g^e = r^{\lambda_e} f_g^e(\varphi) \text{ and } \psi_l^e = r^{\lambda_e} f_l(\varphi), \tag{24}$$

$$f_g^e(\varphi) = A_g^e \cos\lambda_e\varphi + B_g^e \sin\lambda_e\varphi + C_g^e \cos(\lambda_e - 2)\varphi + D_g^e \sin(\lambda_e - 2)\varphi, \tag{25}$$

$$f_l^e(\varphi) = A_l^e \cos\lambda_e\varphi + B_l^e \sin\lambda_e\varphi + C_l^e \cos(\lambda_e - 2)\varphi + D_l^e \sin(\lambda_e - 2)\varphi. \tag{26}$$

The homogeneous system of linear algebraic equations for coefficients of stream functions (25) and (26) would have a nontrivial solution if and only if the system matrix $\mathbf{E}(\lambda_e)$ is singular. Thus, λ_e are found by solving the equation $\det\mathbf{E}(\lambda_e) = 0$. Notably, the determinant of the matrix $\mathbf{E}$ takes a rather simple form

$$\det\mathbf{E} = 8(\lambda - 1)[\mu\mathcal{G}(\lambda,\theta)\mathcal{M}_-(\lambda,\beta) + \mathcal{M}_-(\lambda,\theta)\mathcal{G}(\lambda,\beta)]. \tag{27}$$

In the limiting case, when the gas phase has zero viscosity, the determinant of $\mathbf{E}$ reads

$$\det\mathbf{E}_{\mu=0} = 8(\lambda - 1)\mathcal{G}(\lambda,\beta)\mathcal{M}_-(\lambda,\theta). \tag{28}$$

Note that $\mathcal{M}_-(\lambda,\theta)$ is the function encountered in the studies of Moffatt eddies in the liquid phase [29]. The function $\mathcal{G}(\lambda,\beta)$ in (28) accounts for the changes of the flow in the gas phase, since in the case $\mu = 0$, the flows are decoupled.

All solutions discussed above are obtained for fixed θ while in reality the contact angle in the pinned contact line mode is expected to decrease as the droplet or rivulet loses mass by evaporation. Our treatment here is quasisteady, i.e., based on the assumption that the timescale of such decrease is much slower than the time required to establish local flow structures considered in the present study. Furthermore, we note that the flow solution associated with the contact angle decrease corresponds to $\lambda = 2$ and thus is subdominant when compared to the dominant contributions from either evaporation induced flow or the eigenmode solution, as was also the case in Gelderblom *et al.* [34].

C. Prefactor *K*

All local solutions for evaporative flux discussed above depend on the prefactor K, which can be determined only from the global solution. Here we discuss examples of geometric configurations for which the value can be found without extensive numerical simulations. The order of K for sessile droplets on flat surfaces can be evaluated for an arbitrary contact angle based on the Popov's [46] solution for the distribution of evaporation flux. For low contact angles ($\theta \approx 0$ and $\gamma \approx \pi$) this solution in dimensionless form reads $J_{dr} = \frac{2}{\pi\sqrt{1-R^2}}$, where the radius of the drop footprint is chosen as a length scale and R a dimensionless distance from the droplet symmetry axis. In the vicinity of the contact line this solution reduces to

$$J_{dr} \approx \frac{\sqrt{2}}{\pi\sqrt{r}} = \frac{1}{2}K_{dr}r^{-\frac{1}{2}} \tag{29}$$

with $K_{dr} = \frac{2\sqrt{2}}{\pi} \approx 0.9$.

Equation (29) is applicable not only to evaporation of thin drops from flat substrates, but also to evaporation of liquid from holes of approximately circular cross section, where the liquid is pinned at the edge of the hole. The following relation between the angles should be satisfied: $\beta = 2\pi - \theta - \gamma = \pi$, for example, with $\theta = \frac{\pi}{2}$ and $\gamma = \frac{\pi}{2}$.

The problem of obtaining the prefactor K for parallel straight open channels, even for the cases when $\beta = \pi$, is nontrivial, as it involves solving a complicated mixed boundary value problem. Since the problem with a constant concentration $\rho_{v,\infty}$ at the infinite distance from the liquid-gas interface does not have a solution in this case (in contrast to the axisymmetric configuration solved by Popov [46]), we consider a rectangular domain $\Omega = [0, W] \times [0, H]$, which is the cross section of the open channel geometry considered, with all length variables now scaled by the half-width of the channel. The channel is filled with liquid whose free surface is nearly flat, corresponding to all combinations of γ and θ obeying the relation $\gamma + \theta = \pi$ in terms of our general problem formulated above, for example, $\gamma = \theta = \pi/2$. The steady nondimensional vapor diffusion equation on the domain Ω has the following form:

$$\frac{\partial^2 c}{\partial x^2} + \frac{\partial^2 c}{\partial y^2} = 0, \tag{30}$$

where c is scaled as before and the boundary conditions are the following:

$$c\Big|_{0<x\leqslant 1, y=0} = 1, \ \frac{\partial c}{\partial y}\Big|_{1<x<W, y=0} = 0 \text{ and } c\Big|_{y=H} = 0, \tag{31}$$

$$\frac{\partial c}{\partial x}\Big|_{x=0} = 0 \text{ and } \frac{\partial c}{\partial x}\Big|_{x=W} = 0. \tag{32}$$

The constant concentration at the upper boundary (mass boundary layer) can be justified by assuming that there is a substance absorbing vapor molecules at that location [47]. The solution of Eqs. (30)–(32) in the context of a temperature distribution in a chip was performed elegantly by Bilotti [48] who employed a double Schwarz-Christoffel mapping.

A closed-form solution for the concentration field is possible only for the limiting cases. For example, in the limit $W \to \infty$, corresponding to a single channel, the evaporative flux $J_{ch}(y = 0, x)$ takes a simple form:

$$J_{ch}(x) = \frac{\pi}{2Hk_w \mathscr{K}'_w}\left[\cosh^2\left(\frac{\pi x}{2H}\right) - \frac{1}{k_w^2}\sinh^2\left(\frac{\pi x}{2H}\right)\right]^{-\frac{1}{2}}, \tag{33}$$

where $k_w = \tanh\frac{\pi}{2H}$, and $\mathscr{K}'_w$ is a complete elliptic integral of the first kind with the modulus $k'_w = \sqrt{1 - k_w^2}$. In the vicinity of the contact line Eq. (33) reduces to

$$J_{ch}(x) \approx \frac{1}{2\mathscr{K}'_w\sqrt{r}}\left(\frac{\pi}{Hk_w}\right)^{\frac{1}{2}} = \frac{K_{ch}(H)}{2\sqrt{r}}, \tag{34}$$

where the prefactor K_{ch} reads

$$K_{ch}(H) = \frac{1}{\mathscr{K}'_w}\left(\frac{\pi}{Hk_w}\right)^{\frac{1}{2}}. \tag{35}$$

Further simplification suggested by Bilotti [48] for the case when the far-field concentration is reached far away from the interface, that is $H \to \infty$, is of the form:

$$J^{\dagger}_{ch}(x) = \frac{\pi}{2Hk_w \mathscr{K}'_w}(1 - x^2)^{-\frac{1}{2}}. \tag{36}$$

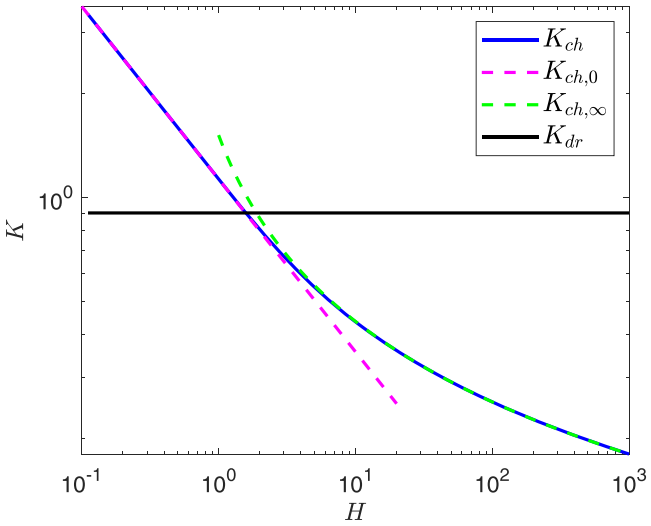

FIG. 2. Evaporation coefficient for a single open channel and for a thin drop.

Taking into account the asymptotic behavior of k_w and $\mathscr{K}_w'$ at $H \to \infty$, one can derive the following asymptotic expression for the prefactor K_{ch}:

$$K_{\mathrm{ch},\infty}(H) = -\frac{\sqrt{2}}{\log\left(\frac{\pi}{8H}\right)}. \tag{37}$$

If the far-field concentration is prescribed close to the interface ($H \to 0$), the following asymptotic expression for the prefactor can be derived:

$$K_{\mathrm{ch},0}(H) = \frac{2}{\sqrt{\pi H}}. \tag{38}$$

In Fig. 2 we plot expressions (35), (37), and (38) in order to illustrate the dependence of the prefactor K_{ch} on the geometry of the system, that is on the ratio between the height of the plane, at which the constant vapor concentration ($\rho_{v,\infty}$) boundary condition is posed, and the half-width of the channel. For comparison, the prefactor for thin drop, K_{dr}, is also shown in the plot. We note that if H is infinitely large, K_{ch} tends to zero, and if H is infinitely small, K_{ch} diverges. Both trends can be explained by observing that scaled concentration gradients in the vertical direction are on the order of $1/H$ since the nondimensional concentration changes from one to zero between the liquid surface and the top boundary. We also note that the asymptotic expressions for large [Eq. (37)] and small [(Eq. (38)] values of H retain good accuracy for the values of H of order one. For $H \approx \pi/2$ the prefactor for evaporation from an open channel is equal to the prefactor for evaporation of thin drop. Equations (35), (37), and (38) are applicable for single straight open channels with an arbitrary cross section, if the liquid-gas interface is flat and the liquid is pinned at the edge of the channel.

III. RESULTS AND DISCUSSION

A. Critical and pseudocritical angles

Since the flow in the vicinity of the contact line for either a droplet or a rivulet is a superposition of the solutions obtained above. Either an evaporation-induced flow solution or an eigenmode solution will dominate the flow. It is of interest, hence, to generalize the results presented by Gelderblom *et al.* [34] and recently by Ajaev and Kabov [40] to the case of a contact line pinned at the wedge and determine critical contact angles θ_C at which the dominating contribution changes. Of

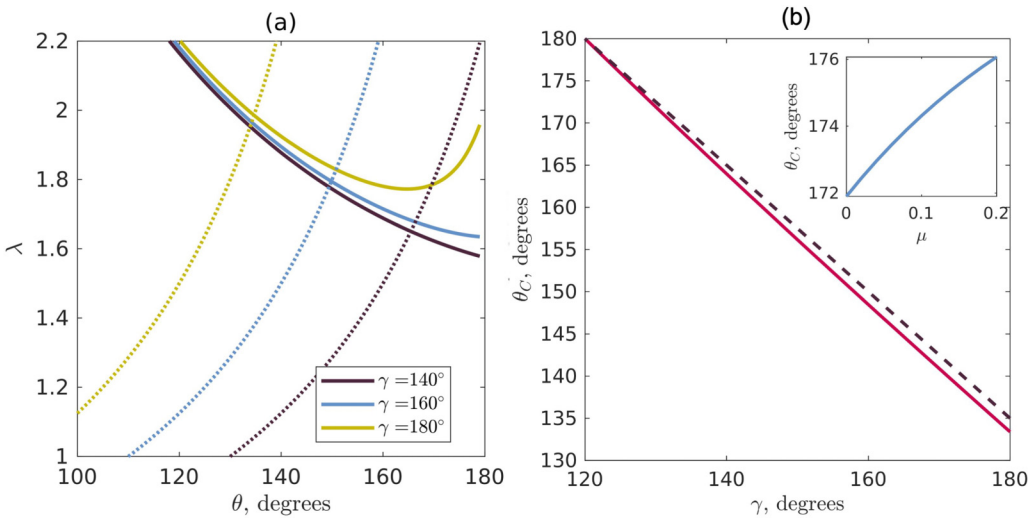

FIG. 3. The critical angles when the dominating flow contribution changes evaluated for different λ. (a) Dependence of λ on the contact angle θ. The solid lines represent the eigenmode solution and the dotted ones the evaporation-induced flow solution. The viscosity ratio is $\mu = 0.05$. (b) Dependence of the critical contact angle θ_C on the solid wedge angle γ predicted by the approximate linear model (dashed line) for $\mu = 0$ and the numerical solution (solid line), with inset showing a typical dependence of the same quantity on μ.

particular interest is how the Stefan flow affects the critical angles and the transition flow structure when θ is around θ_C.

In Fig. 3(a) the dependence of λ for both evaporation-driven and eigenmode solutions on the liquid contact angle θ for different solid angles γ is illustrated. Numerical solution for λ_e is obtained by applying `fzero` subroutine from Matlab to the determinant from Eq. (27). The flow regime with the smallest λ contributes the most to the flow structure and hence the intersection of two curves (dotted and solid) defines the critical contact angle θ_C. For $\theta < \theta_C$, the evaporation-induced flow solution will dominate the overall flow, otherwise the contribution of the eigenmode solution will be more significant. The critical contact angle increases as a solid opening angle decreases.

For the limiting case of $\mu = 0$, λ_e can be found by setting the determinant from Eq. (28) to zero. The form of the local solution we are using here implies $\lambda \neq 1$ and the function $\mathcal{G}(\lambda, \beta)$ does not contribute to the solution, so we focus on the condition when $\mathcal{M}_-(\lambda, \theta)$ is zero. Detailed analysis of this condition in Dean and Montagnon [28] suggests that for critical angles θ close to π, the value of $(\lambda - 1)\theta$ is near $\pi/2$, leading to an approximate condition of $\lambda_e\theta = 3\pi/4$. This condition turns out to be a reasonable approximation for a range of contact angles, reflecting the fact that the average of θ and $(\lambda - 1)\theta$ varies only in a very narrow range even when θ is no longer close to π. Combining this conclusion with the critical angle condition, $\lambda_e = 2\pi/\beta$, leads to the following simple linear approximation:

$$\theta_C = \frac{3}{2}\left(\pi - \frac{\gamma}{2}\right). \tag{39}$$

A more accurate approximation of dependence of the critical contact angle on γ at $\mu = 0$ can be obtained from numerically finding zeros of the function $\lambda_e - 2\pi/\beta$ (with $\mathcal{M}_-(\lambda_e, \theta) = 0$), an equivalent of finding the intersection points between curves such as the ones shown in Fig. 3(a). We start by evaluating this function on a relatively coarse mesh of 100 points in θ to identify the interval on which it changes sign. Next, the standard Matlab subroutine `fzero` is used to pinpoint the exact location of the zero. Repeating the procedure for different values of gamma results in the solid line in Fig. 3(b). The range of γ chosen in the plot is motivated by the fact that values of either γ or

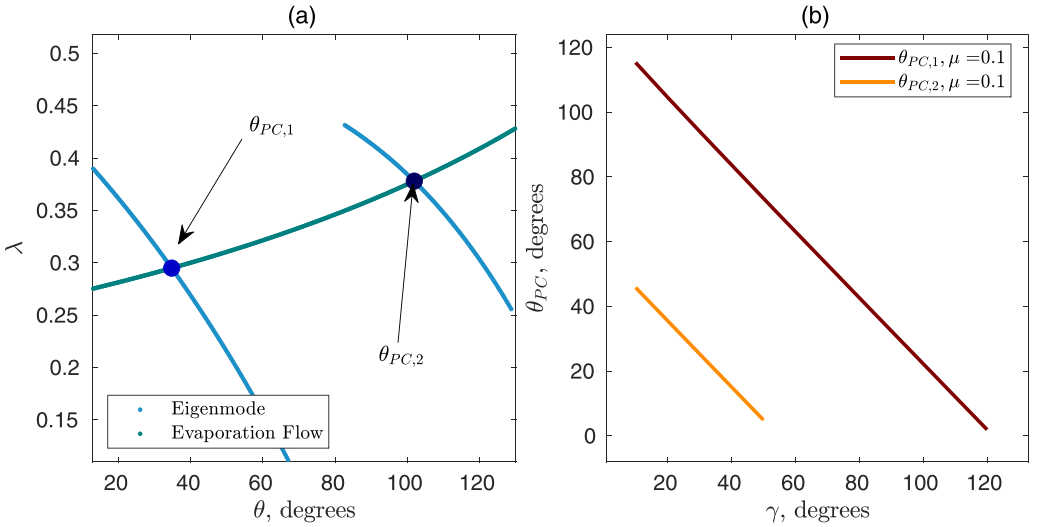

FIG. 4. The pseudocritical angles evaluated for $\lambda \in (0, 1)$: (a) Dependence of λ on the contact angle of a liquid θ when $\gamma = 20^\circ$, $\mu = 0$. The viscosity ratio is $\mu = 0$. (b) Dependence of the critical contact angles θ_C on the solid structure angle.

θ above 180° are not likely to be relevant for typical physical experiments, although we verified that the general trend continues outside the range shown. Remarkably, the dashed line in Fig. 3(b), corresponding to Eq. (39), gives a good approximation of the numerical result over a wide range of angles. Furthermore, when similar numerical procedure is used to find θ_C for nonzero μ, it only produces a small correction for realistic values of μ, as illustrated by the inset in Fig. 3(b). Thus, the simple linear function given by Eq. (39) provides a good approximation for a range of critical contact angles and realistic values of μ.

The critical contact angles θ_C are those near which the dominating flow contribution changes. Mathematically, it corresponds to combinations of θ, γ and $\lambda > 1$ which make the matrix defined by Eq. (19) singular. However, not every such combination leads to a critical value of the contact angle. The complicated nature of the function $\det \mathbf{E}(\lambda, \theta, \gamma)$ leads to many zeros which do not correspond to changes in the dominant flow contribution but can still have important implications for the flow structure, as discussed below in the context of separatrix formation. Indeed, one can see in Fig. 4(a) that as the contact angle decreases the matrix $\mathbf{E}$ can turn singular more than once. The values of λ corresponding to $\det \mathbf{E}(\lambda) = 0$ for those cases are smaller than unity. Therefore, there is no change in the dominant flow contribution, but the streamline pattern change is still expected. We further refer to those angles as pseudocritical and denote them θ_{PC}, as is in Fig. 4. The dependence of the pseudocritical angles on the solid opening angle is close to linear for both $\theta_{PC,1}$ and $\theta_{PC,2}$ [Fig. 4(b)]. One can see that the pseudocritical angles decrease with nearly the same slope as the solid structure flattens and disappear one after another at certain γ. The simple dependence shown allows for a prediction at which solid opening angle only one pseudocritical angle exists and at which solid angle both of them vanish. Similarly to critical angles, pseudocritical angles increase slightly when viscosity of the gas phase is taken into account.

For the case $\mu = 0$, only the flow in the gas phase is expected to change when passing the pseudocritical points with $\theta_{PC} < \theta_M = 73.15^\circ$. That is because for $\theta_{PC} < \theta_M$, no real solutions of equation $\mathcal{M}_-(\lambda, \theta) = 0$ exist. We note that only the solution branches with the smallest λ are depicted in Figs. 3 and 4.

B. Separatrices

Important topological traits of the flow structure are separatrices rendering two or more regions of flow, at least one of which has a recirculation. Thus, the appearance of a separatrix signals a change in the global flow structure, an important motivation for studies of local solutions, especially in the context of heat transfer applications. An emerging or vanishing separatrix implies that the shear stress is zero at the liquid-solid interface and hence $\frac{\partial v_r}{\partial \varphi} = 0$ there [34]. In the case when only flow structure in liquid is considered ($\mu = 0$) and the substrate is flat and rigid, a system of four equations can be solved to obtain a separatrix function $p(\theta) = \sin(\lambda - 2)\theta - \sin\lambda\theta$ [34]. The zeros of this function determine the values of the contact angle at which a new separatrix appears. In order to gain the understanding of the flow structure in both phases in a more general case considered here, we introduce two functions:

$$\mathrm{Sep}_g(\theta, \gamma, \rho, \mu) \equiv \mathrm{Sep}_g = \left.\frac{\partial^2 \psi_g}{\partial \varphi^2}\right|_{\varphi=\beta} \text{ and } \mathrm{Sep}_l(\theta, \gamma, \rho, \mu) \equiv \mathrm{Sep}_l = \left.\frac{\partial^2 \psi_l}{\partial \varphi^2}\right|_{\varphi=-\theta}. \quad (40)$$

Zeros of Sep_g and Sep_l are the angles at which a separatrix in a gas and liquid phase, accordingly, emerges or vanishes at the solid, assuming that the evaporation-induced flow solution dominates. A closed form of those functions is determined by the analytical expressions for the coefficients A_l, B_l, C_l, D_l, A_g, B_g, C_g, and D_g listed in the Appendix, although the zeros of the two functions have to be found numerically due to the transcendental nature of the equations for θ which emerge from (40).

Comparison of $p(\theta)$ and Sep_l for the case $\gamma = 180^\circ$, $\mu = 0$ reveals that they have the same zeros [Fig. 5(a)]. This is not surprising since taking into account a non-viscous gas ($\mu = 0$) should not change the liquid flow structure. It can be seen from the Fig. 5(a) that the liquid separatrix function Sep_l at $\gamma = 180^\circ$ becomes discontinuous at the critical angle θ_C (marked by a dashed line). A separatrix in the liquid phase appears at an angle $\theta < \theta_C$ corresponding to a zero of Sep_l, then moves toward the liquid-gas interface with increasing θ, reaching the interface at $\theta = \theta_C$. This value is when the local solution described above breaks down and the separatrix disappears, as was previously noted by Gelderblom *et al.* [34].

Let us now discuss the emergence of separatrices in the liquid flow when the contact line is pinned at a wedge rather than a flat substrate, starting with the case of $\mu = 0$. When the solid angle γ decreases, the critical angle θ_C increases and the zeros of Sep_l shift to the right, as clearly seen in Fig. 5(b). Note that the critical angles correspond to the locations of the vertical asymptotes, shown by the dashed lines, while the locations where separatrices emerge are the points of intersection of the curves with the horizontal axis. Similar to the case of the flat substrate, the separatrices emerge at $\theta < \theta_C$ and disappear at the critical angle. Note that both the zeros of Sep_l and the critical contact angles shift to the right when γ is decreased. Here we focus on zeros of Sep_l at $\theta < \theta_C$ since the definition of separatrix function is based on the evaporation-induced flow solution which is dominant only below the critical angle.

Similarly to Sep_l, the curve Sep_g intersects the θ axis right before θ_C, leading to a separatrix in the gas phase. As γ decreases, the function Sep_g finds additional intersections with the abscissa axis, leading to possibility of additional separatrix in the gas phase [Fig. 5(c)]. The angle at which the separatrix emerges increases as γ decreases. The cases of acute solid angles γ are depicted in Fig. 5(d). One can see that, as predicted above, two pseudocritical angles are present in the case $\gamma = 40^\circ$ and one in the case $\gamma = 80^\circ$. Two separatrices are expected for $\gamma = 40^\circ$ around the second pseudocritical angle as well around the first pseudocritical angle for $\gamma = 80^\circ$. Zeros of the separatrix function are attained near the pseudocritical angles.

The situation becomes more complicated when the flows in the liquid and gas phase are coupled, that is the case when $\mu \neq 0$. In Fig. 6 the behavior of the functions Sep_l and Sep_g for $\mu = 0.1$ is compared to those with $\mu = 0$ for the obtuse angle of $\gamma = 160^\circ$ and the acute angle of $\gamma = 40^\circ$. The dark blue lines in Fig. 6(a) correspond to the same separatrix function as Fig. 5(b) except that different vertical scale makes parts of the graph appear as vertical lines. It is immediately clear that increasing the viscosity ratio to $\mu = 0.1$ drastically changes the shape of the separatrix function.

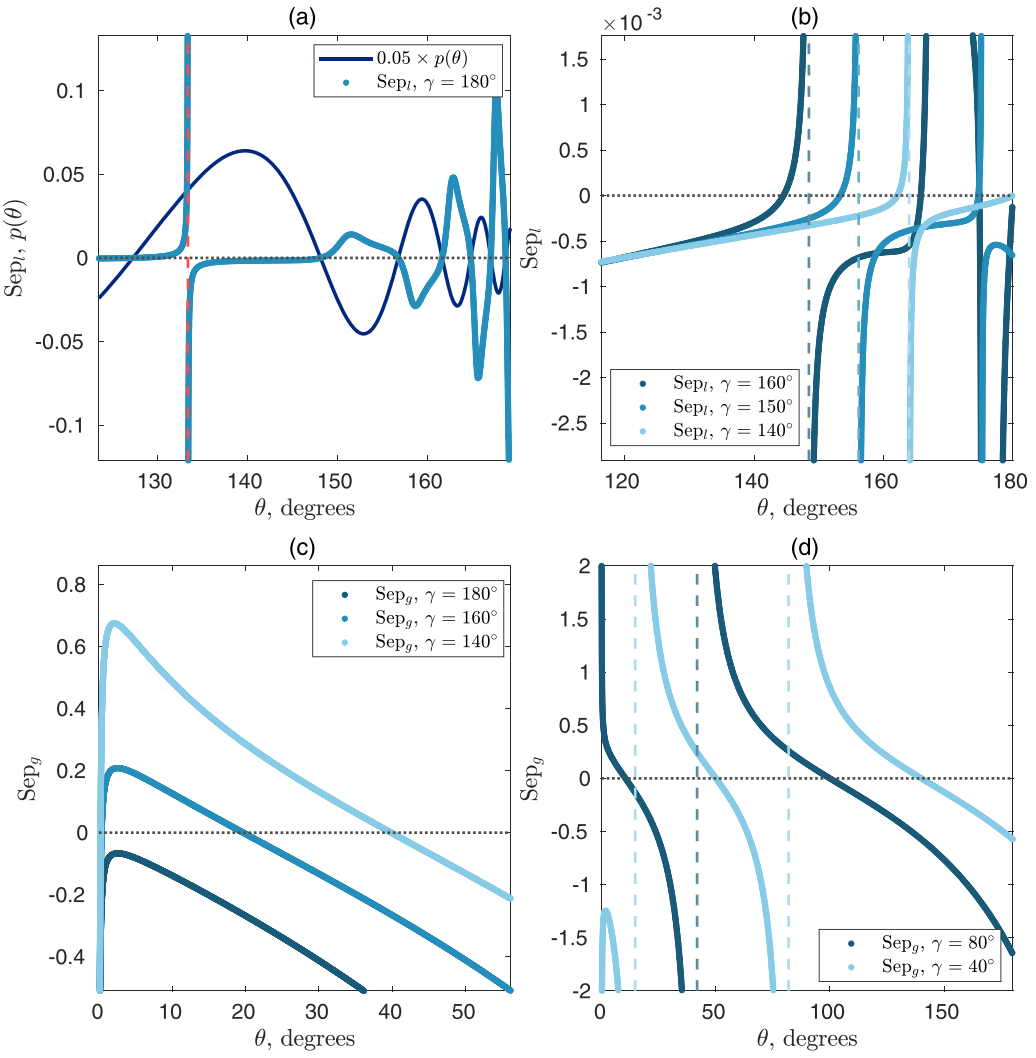

FIG. 5. The separatrix functions Sep_g and Sep_l: (a) The separatrix function Sep_l (circle markers) for the case $\gamma = 180°$, $\mu = 0$ compared to the function $p(\theta)$ (solid line) obtained by Gelderblom *et al.* [34]; (b) The separatrix function Sep_l for solid angles $\gamma = 140°, 150°, 160°$; (c, d) The separatrix functions in a gas phase Sep_g for different γ. Dashed lines are to show the discontinuous behavior corresponding to the critical and pseudocritical angles. The dotted black line depicts the abscissa axis.

Most importantly, when the gas phase is viscous, no separatrix in the liquid phase accompanies the critical angle in contrast to the case $\mu = 0$, as seen by comparing Fig. 6(a) and Fig. 5(b). Such a change implies that there is likely a threshold value of the viscosity ratio, above which no separatrix in the liquid phase can be observed for $\theta < \theta_C$. To determine if that is the case, let us plot the separatrix function around θ_C for the liquid phase for the different ratios of viscosity. In Fig. 7 one can see that as the viscosity ratio increases, the separatrix function shifts to the region of higher contact angles and eventually passes the critical angle θ_C. That means that for a larger gas viscosity a separatrix will appear not before but after the critical point. In its turn, for the very small viscosity ratios, no effect on the flow around the critical angle is expected to be observed and the angle θ_s, at which the separatrix appears, does not change noticeably compared to the case of the decoupled

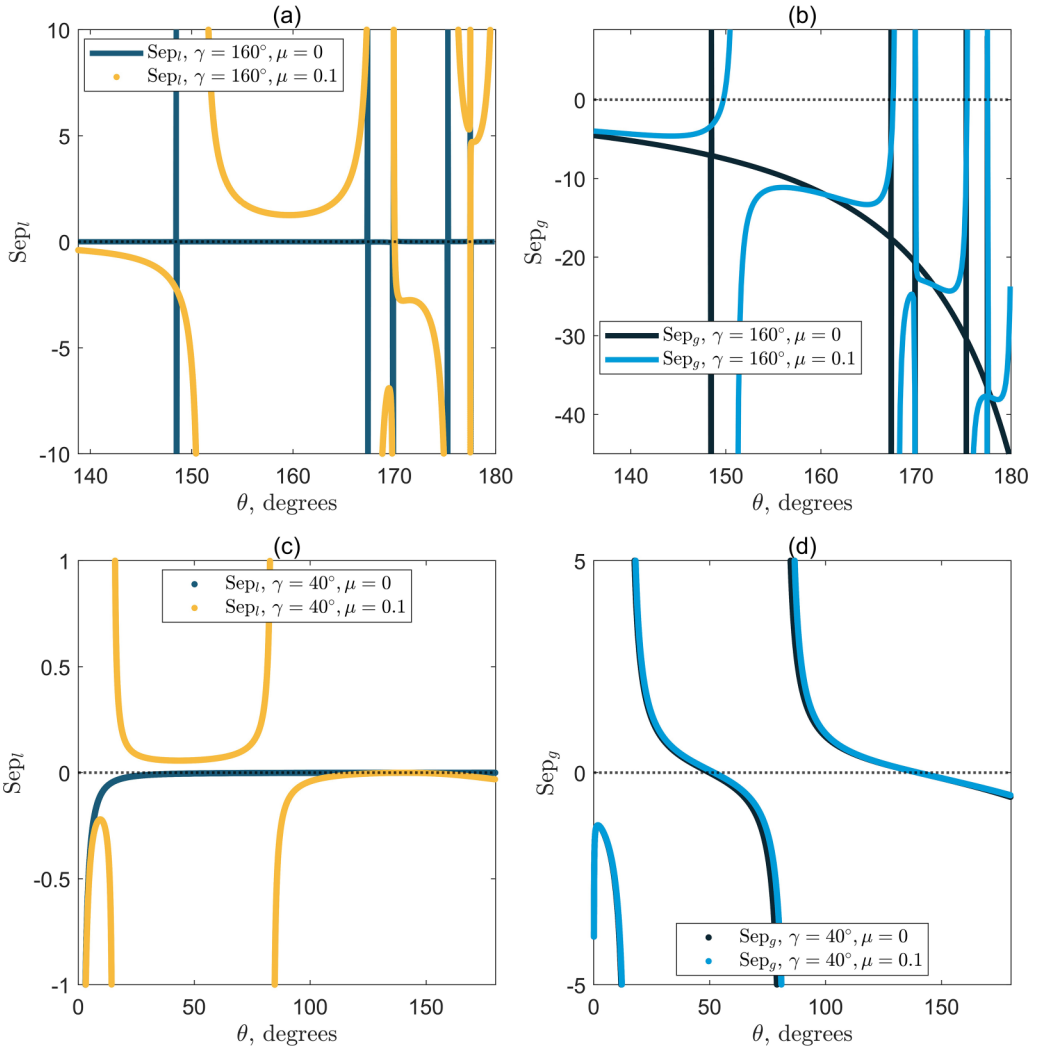

FIG. 6. The separatrix functions Sep_g and Sep_l for the obtuse angle of $\gamma = 160°$ and the acute angle of $\gamma = 40°$. The orange markers in (a) and (c) as well as light blue markers in (b) and (d) are for the case when $\mu = 0.1$. The dotted black line depicts the abscissa axis.

flows. The separatrix (and hence θ_s) first starts to shift after $\mu \sim 10^{-6}$ is reached [Fig. 7(b)]. It may seem surprising that such a small change in gas viscosity can eliminate the separatrix. A possible physical explanation is as follows. Since liquid is not crossing the separatrix, the local liquid velocity direction should be parallel to the direction of the separatrix itself. This implies that the local shear stress should be vanisingly small and thus unable to match the shear stress from the flow in the gas phase, making formation of a separatrix impossible unless the shear stress from the gas phase is also very small, which is indeed the case when $\mu \to 0$.

A separatrix in the gas phase when the flows are coupled appears right before the critical angle θ_C is reached, whereas when $\mu = 0$ it sprouts immediately after it [Fig. 6(b)]. For the acute angles, increasing the viscosity ratio has a much weaker effects on the zeros of Sep_l and of Sep_g, although the shape of the separatrix functions still changes [Figs. 6(c) and 6(d)].

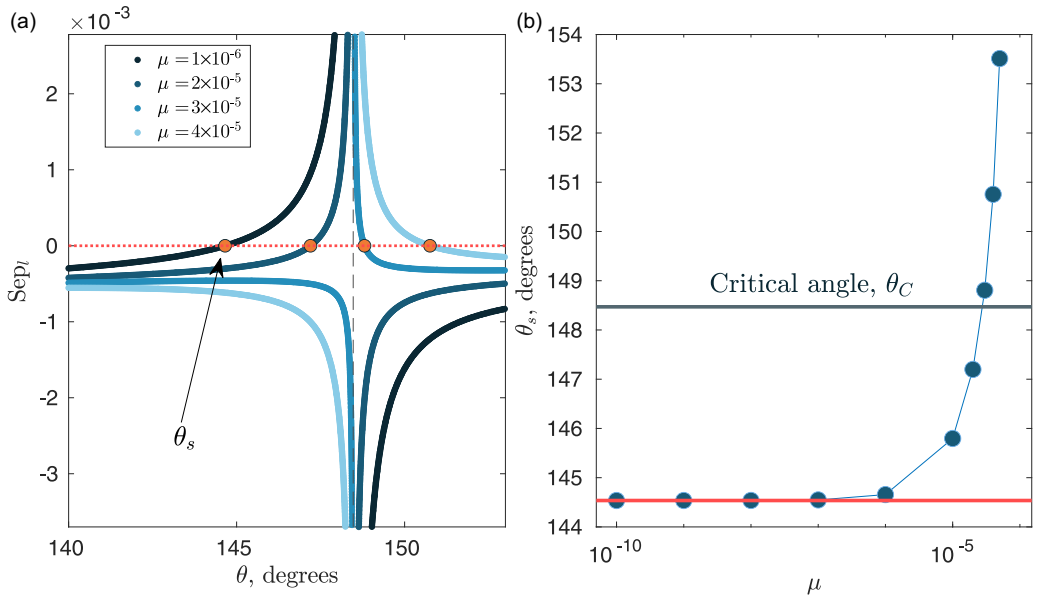

FIG. 7. Influence of the viscosity ratio μ on the flow in a liquid phase for $\gamma = 160^\circ$: (a) behavior of separatrix function Sep_l at different values of the viscosity ratio; (b) effect of the viscosity ratio on the separatrix angle θ_s emerging in the vicinity of the critical angle θ_C. The dashed line in (a) is to approximately show the location of θ_C (here taken as 148.47°), the red dotted line is to show the abscissa axis. The orange circle markers are to show θ_s, the angles where a separatrix is to emerge (as is shown by the arrow). The red line in (b) is to depict the value of θ_s for $\mu = 0$; the black line is to approximately show the location of θ_C (here taken as 148.47°).

C. Flow structure

Now, as the machinery for characterizing the flow is described, let us turn our attention to the flow structure. We first consider the local liquid phase streamline pattern for a droplet on a flat rigid surface and $\mu = 0$ to validate our solutions by comparison with Gelderblom *et al.* [34]. Consistent with their results, a separatrix is seen in Fig. 8 at $\theta = 130^\circ$, but it disappears at $\theta = \theta_C$, so it is no longer seen in the other five liquid flow patterns in Fig. 8. Taking the limit of μ does not completely decouple the flows in the two fluid phases since the tangential velocity is still assumed continuous at the liquid-air interface, but it does allow us to first determine the flow patterns in the liquid and then use the result to describe the air flow streamlines, which are also represented in Fig. 8. The increase of the liquid separatrix angle is accompanied by curling of the flow in the gas phase. When the contact angle is $\theta \approx 133.3899^\circ$, the recirculation of the flow in the gas phase is observed. The flow in the liquid phase is directed along the interfaces as well. Those structures can only be observed in a very narrow range of contact angles. As the angle increases, a separatrix appears in the gas phase ($\theta \approx 133.3905^\circ$). That has been already suggested from the behavior of the function Sep_g discussed above. The separatrix reaches the solid-liquid interface so that the recirculation in the gas disappears already at $\theta = 133.4^\circ$ reported to be a critical angle [34]. Further increase of the contact angle renders the air flow with the streamlines nearly orthogonal to the liquid-air interface. The intensity of the evaporation in the vicinity of the contact line, as expected, is very low when θ is large. Consequently, the fan of separatrices (not shown here) appears in the liquid phase in agreement with the predictions in Fig. 5(a) and the results in [34]. One, however, should keep in mind that for $\theta > \theta_C$ the evaporation-induced flow is subdominant.

Let us now discuss flow patters when the substrate is no longer flat. As the solid opening angle γ decreases, the flow structure in both liquid and gas phases changes. One can see from Fig. 5(c) that

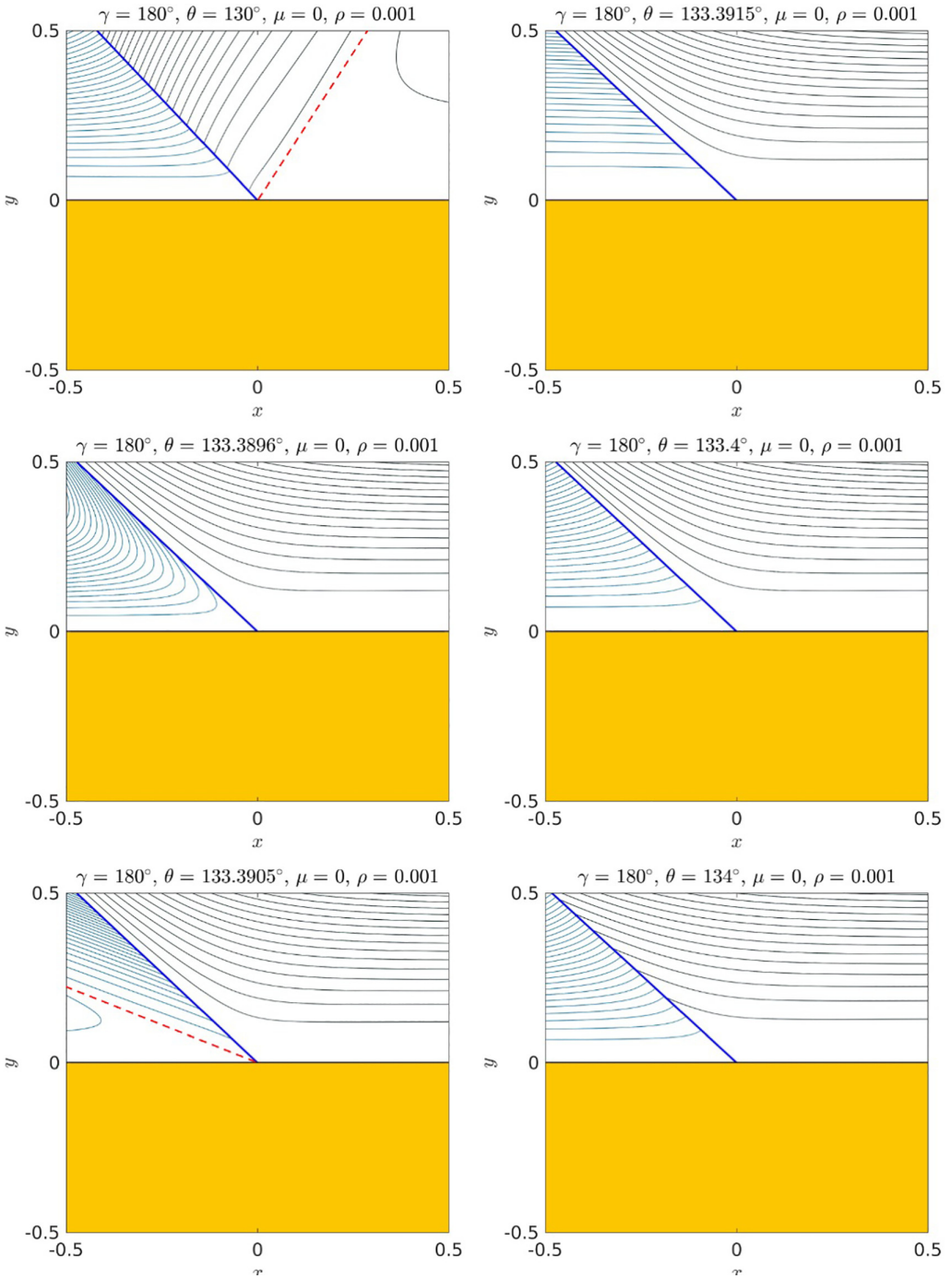

FIG. 8. The flow structures obtained for the solid opening angle $\gamma = 180°$ for the limiting case of $\mu = 0$. Black and blue stream lines correspond to the liquid and gas phase; accordingly, the orange-filled regions correspond to the solid phase where no flow occurs. Red dashed lines schematically depict the separatrices.

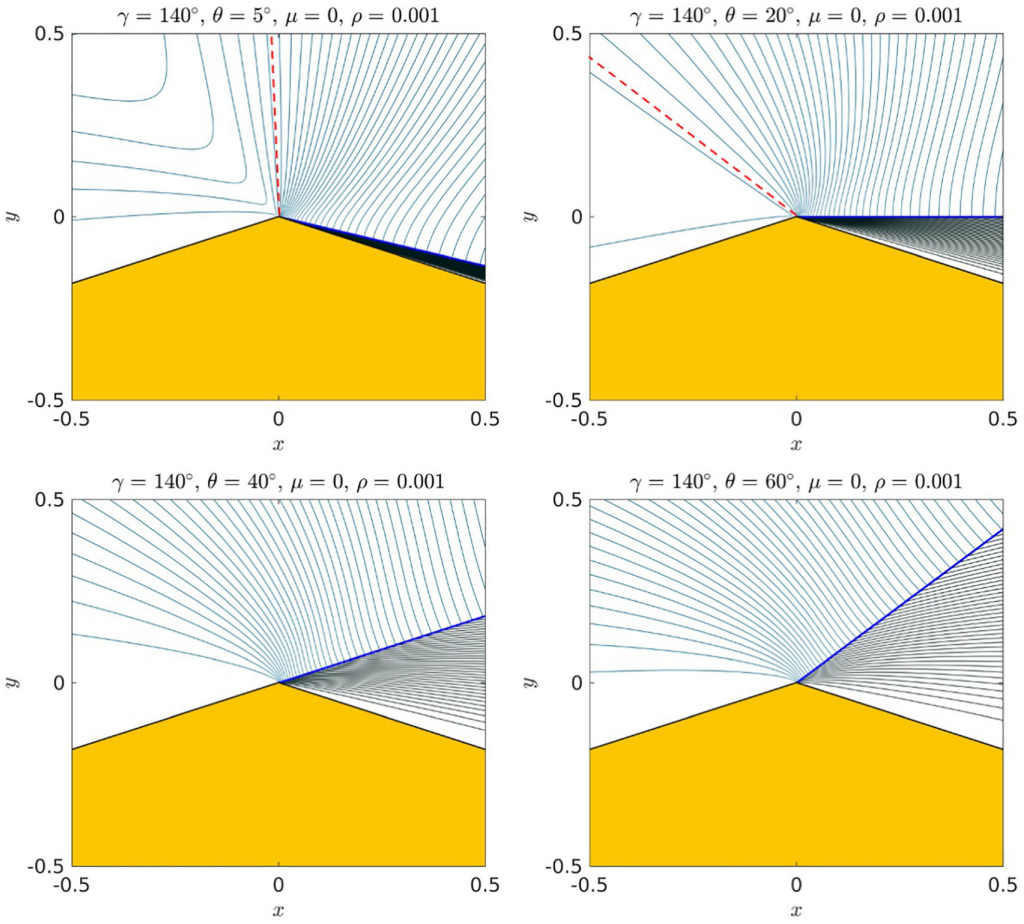

FIG. 9. The flow structures obtained for the solid opening angle $\gamma = 140^\circ$ for the limiting case of $\mu = 0$. Black and blue stream lines correspond to the liquid and gas phase, accordingly; the orange-filled regions correspond to the solid phase where no flow occurs. Red dashed lines schematically depict the separatrices.

for $\gamma < 180^\circ$ the function Sep_g can intersect an abscissa axis at small contact angles, indicating a separatrix in the gas phase. In Fig. 9 that is illustrated for the solid angle $\gamma = 140^\circ$. When the contact angle is small, a flow in the gas phase consists of two regions, one of which shows recirculation. If the contact angle of the liquid increases, the angle β decreases accordingly and the recirculation starts becoming "displaced." Eventually, when $\theta \approx 40^\circ$, the separatrix vanishes and the streamlines of the gas flow end at the liquid-gas interface. The flow in the liquid is directed towards the interface as well and is more intense for smaller θ.

For even smaller acute solid angles γ, one expects significant changes in the flow structure in the gas phase as indicated by plotting Sep_g in Fig. 5(d) while the flow in the liquid phase is to be hardly altered. In Fig. 10 the flow structures for $\gamma = 40^\circ$ and $\mu = 0$ are illustrated. It can be indeed seen that the flow in gas phase has a rather complex structure with several regions divided by separatrices. When passing the first pseudocritical angle $\theta_{PC} \approx 14.81^\circ$, the direction of the stream lines at the liquid-gas interface changes and when $\theta \approx 50.11^\circ$ the separatrix vanishes (Fig. 10, the right column).

In the real-world scenarios, the viscosity of the gas phase is never zero and, hence, the flows in the liquid phase and gas phase are coupled through the shear stress balance. In the following, we,

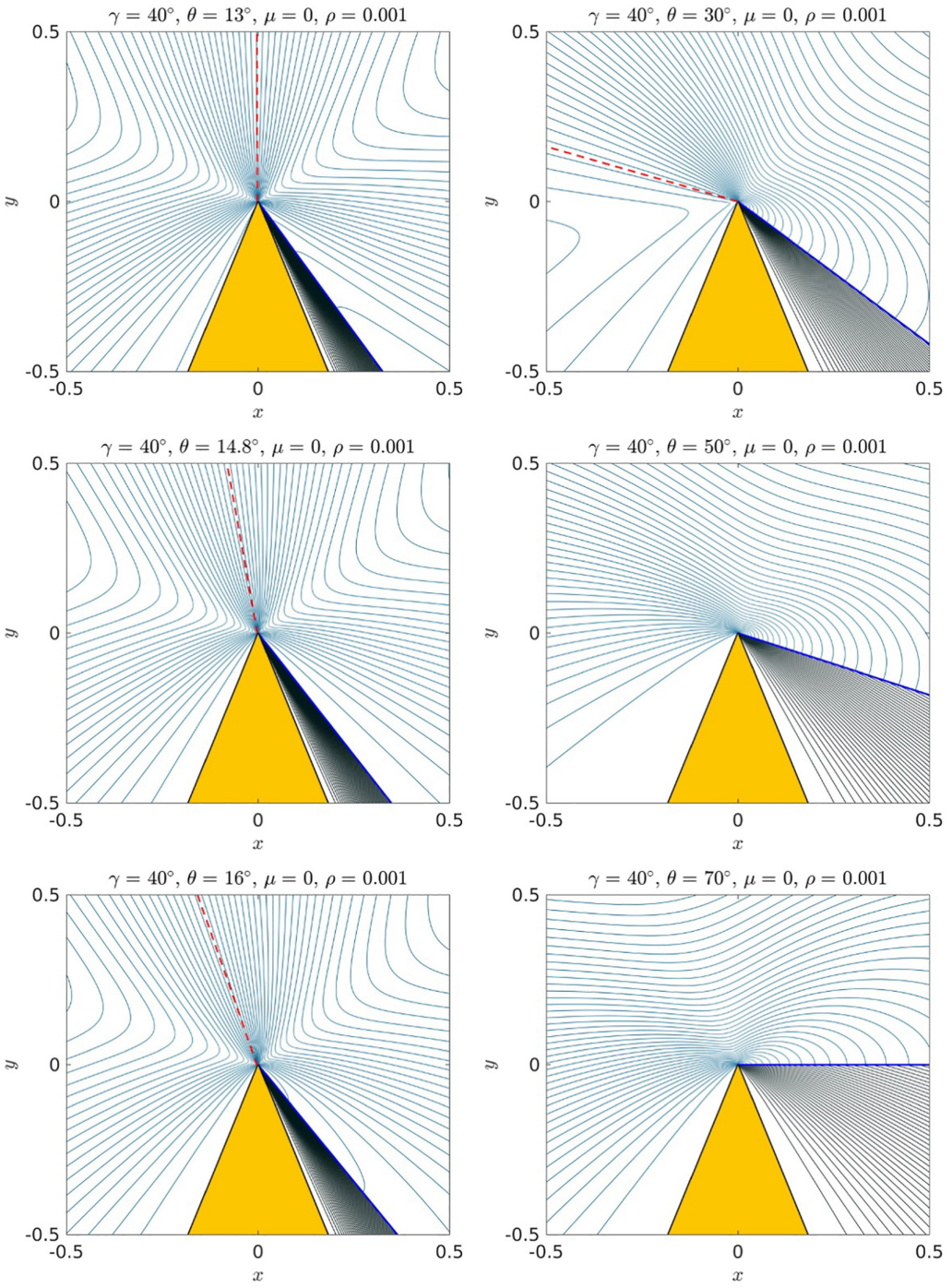

FIG. 10. The flow structures obtained for the solid opening angle $\gamma = 140^\circ$ and $\mu = 0$. Black and blue stream lines correspond to the liquid and gas phase, accordingly, the orange-filled regions correspond to the solid phase where no flow occurs. Red dashed lines schematically depict the separatrices.

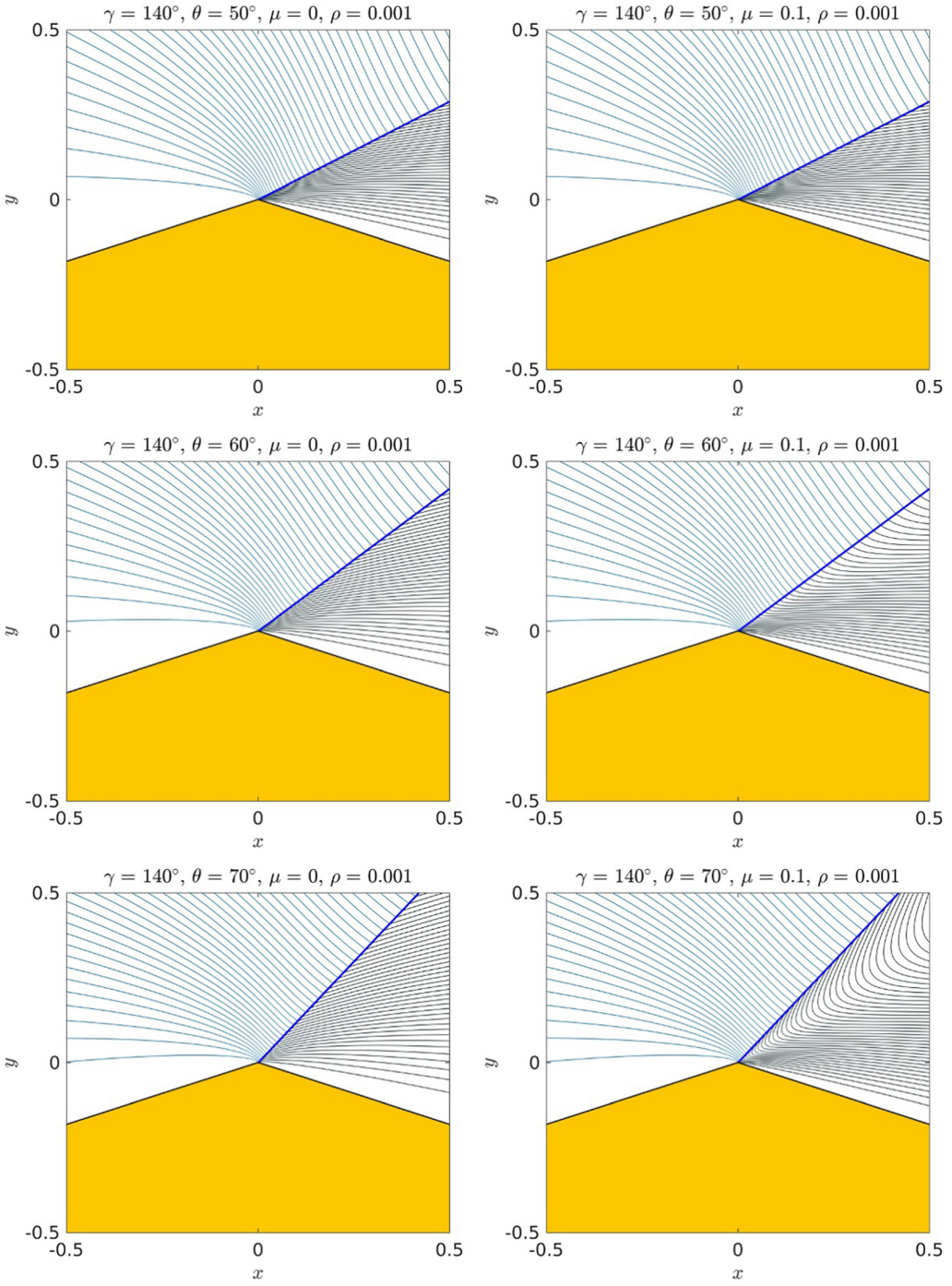

FIG. 11. The flow structures obtained for the solid opening angle $\gamma = 140°$. The case when the gas is nonviscous $\mu = 0$ corresponds to the left column and a viscous gas $\mu = 0.1$ corresponds to the right column. Black and blue stream lines correspond to the liquid and gas phase; accordingly, the orange-filled regions correspond to the solid phase where no flow occurs.

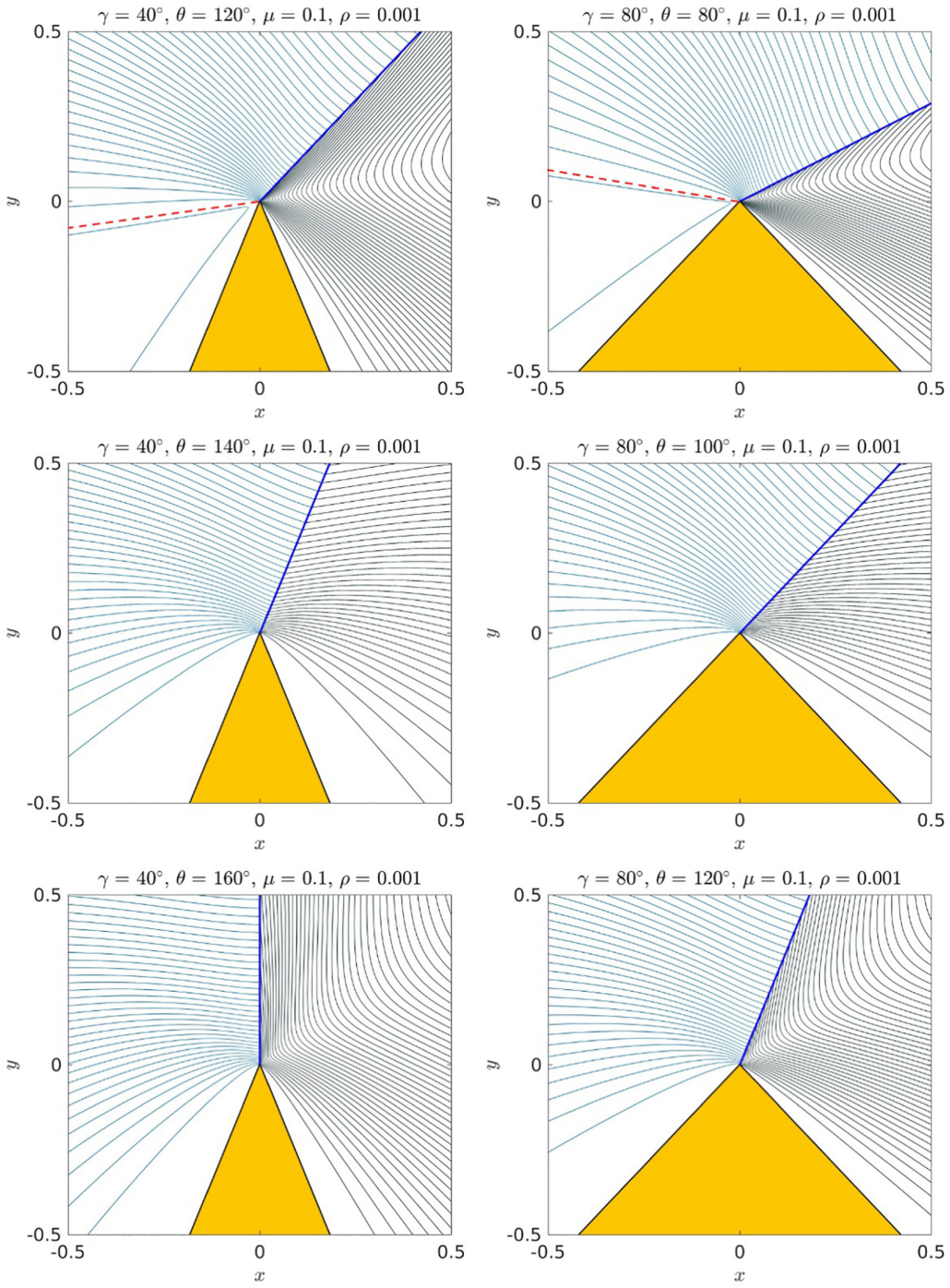

FIG. 12. The flow structures obtained for the solid opening angle $\gamma = 40°$ (left column) and $\gamma = 80°$ (right column) around θ when a separatrix in the gas phase vanishes. Black and blue stream lines correspond to the liquid and gas phase; accordingly, the orange-filled regions correspond to the solid phase where no flow occurs. Red dashed lines schematically depict the separatrices.

hence, analyze how taking the viscosity of a gas phase into account can change the flow topology. The flow structures for $\gamma = 140^\circ$ for $\mu = 0$ and $\mu = 0.1$ are presented in Fig. 11 for the contact angle range $\theta \in [50^\circ, 70^\circ]$. No separatrices or critical points belong to that range for either of the viscosity ratios μ and, thus, no conclusion on the flow structure can be drawn exclusively either from the functions Sep_g and Sep_l or from the locations of peculiarities. One can see that no noticeable differences between flows with two viscosity ratios $\mu = 0$ and $\mu = 0.1$ are present for $\theta = 50^\circ$ (and less). The flow in the liquid phase has both normal and tangential velocity components. Yet, when the gas phase is viscous, the flow in the liquid phase starts being altered as the contact angle increases. At $\theta = 60^\circ$, the tangential velocity component nearly disappears and the flow is directed normally towards the liquid-gas interface. After that, at the further contact angle increase ($\theta = 70^\circ$), the direction of the flow changes as it curls and the tangential velocity component overpowers the normal one. This flow structure with the streamlines running along the interfaces remains until the contact angle reaches the value of $\theta \approx 170^\circ$. Interestingly, no noticeable differences in the flow in the gas phase are observed between the cases with $\mu = 0$ and $\mu = 0.1$.

Additionally, it is curious that emergence or vanishing of separatrix in the gas phase seems to affect the flow in the liquid phase. Such alterations are depicted in Fig. 12. It can be seen that before and after the point where a separatrix in the gas phase disappears, the flow in the liquid phase has a much larger tangential velocity than the normal one. At the vicinity of the point where a separatrix in the gas vanishes, the flow in the liquid is directed normally to the liquid-gas interface. No such influence is observed when the flows are decoupled or the viscosity ratio is small.

IV. CONCLUSIONS

We have considered the evaporation of droplets and rivulets occurring on complex surfaces and obtained the local solutions for the flows in both liquid and gas phases in the vicinity of the contact line. Such local solutions are known to have three contributions: evaporation-induced flow, an eigenmode solution corresponding to homogeneous boundary conditions, and flow due to gradual mass loss due to evaporation [34]. We generalized the previous studies of these solutions by considering a contact line pinned at a protruding wedge instead of a flat surface and taking into account the flow in the gas phase. The critical contact angle θ_C above which the eigenmode solution overtakes the evaporation-induced flow as the dominant contribution is found to decrease with increase of the wedge angle γ and increase as the gas-to-liquid viscosity ratio μ is increased. An approximate model is developed in the limit of small μ which leads to a simple analytical expression for the contact angle as a function of γ shown to be in good agreement with the more general formulas.

A separatrix in the liquid flow at $\mu = 0$ was found near the critical value of θ_C in the previous study of Gelderblom *et al.* [34]. For the wedge angles γ below 180°, we found that the separatrix appears at higher values of θ, but can be completely suppressed by increasing the value of the gas phase viscosity. Thus, predictions of flow structures based on the limiting case of $\mu = 0$ may not be possible to observe in experiments, since gas viscosity is never exactly zero. Decreasing γ also can lead to emergence of new separatrices in the gas phase.

Evaporation of droplets and rivulets on nonplanar surfaces is more complex than on flat substrates and is rarely analytically treatable. The local solutions obtained in the present study can serve as a powerful tool to give insights into flow patterns in droplets or rivulets, as well as to provide useful validation tests for the computational studies of these important problems. In particular, the appearance of separatrices in the local liquid phase solutions suggests that there is at least one recirculation region in the cross section of an axisymmetric droplet. If colloidal particles are present in the liquid, they will be recirculating in that region rather than being carried to the droplet surface. Separatrices in the gas flow provide insight into convective flow structure in the gas phase, which is known to affect global heat transfer rates.

While local solutions provide many usefuls insights into the flow structure, it is important to note their limitations. In particular, our focus on the dominant contribution to the local solution does

not allow us to determine the rate of decrease of the contact angle as evaporation progresses or the contribution of Marangoni stresses to the flow structure. These effects are coupled to evaporation and could only be described by a combination of local analyses and computational studies.

ACKNOWLEDGMENTS

The authors gratefully acknowledge financial support from the Deutsche Forschungsgemeinschaft (DFG, German Research Foundation) in the framework of the Priority Program "Dynamic Wetting of Flexible, Adaptive and Switchable Surfaces" (SPP 2171), Project ID 422792679, as well as in the framework of CRC 1194, Project ID 265191195, subproject A04.

APPENDIX: ANALYTICAL SOLUTION FOR THE COEFFICIENTS OF STREAM FUNCTIONS

Provided the auxiliary functions (20)–(23), the solution for the coefficients of stream functions ψ_g and ψ_l reads

$$A_g = -\frac{\lambda K\rho\mathcal{M}_-(\lambda,\beta)[\mathcal{G}(\lambda,\theta)+\mathcal{H}_-(\lambda,\theta)+2]}{2\mu\mathcal{G}(\lambda,\theta)\mathcal{M}_-(\lambda,\beta)+2\mathcal{M}_-(\lambda,\theta)\mathcal{G}(\lambda,\beta)} + \frac{K(\lambda-2)[\mu\mathcal{G}(\lambda,\theta)\mathcal{M}_-(\lambda,\beta)+\mathcal{H}_+(\lambda,\beta)\mathcal{M}_-(\lambda,\theta)]}{2\mu\mathcal{G}(\lambda,\theta)\mathcal{M}_-(\lambda,\beta)+2\mathcal{M}_-(\lambda,\theta)\mathcal{G}(\lambda,\beta)}, \tag{A1}$$

$$D_g = -K\lambda\frac{-\mathcal{P}(\lambda)\mathcal{H}_+(\lambda,\beta)-2\mu\lambda(\lambda-2)+(\lambda-1)\cos 2\theta[(\mathcal{H}_+(\lambda,\beta)+2)(\lambda-1)\mu-\mathcal{H}_+(\lambda,\beta)(\lambda-2)\rho]}{2\mu\mathcal{G}(\lambda,\theta)\mathcal{M}_-(\lambda,\beta)+2\mathcal{M}_-(\lambda,\theta)\mathcal{G}(\lambda,\beta)} + K\lambda\frac{\mu(\mathcal{H}_+(\lambda,\beta)+2)\cos 2\theta(\lambda-1)+\mathcal{M}_-(\lambda,\theta)\mathcal{M}_+(\lambda,\beta)}{2\mu\mathcal{G}(\lambda,\theta)\mathcal{M}_-(\lambda,\beta)+2\mathcal{M}_-(\lambda,\theta)\mathcal{G}(\lambda,\beta)}, \tag{A2}$$

$$A_l = \frac{K(\lambda-2)[\mathcal{H}_+(\lambda,\theta)\mathcal{M}_-(\lambda,\beta)\mu\rho+\mathcal{M}_-(\lambda,\theta)\rho\cos 2\beta(\lambda-1)]}{2\mu\mathcal{G}(\lambda,\theta)\mathcal{M}_-(\lambda,\beta)+2\mathcal{M}_-(\lambda,\theta)\mathcal{G}(\lambda,\beta)} + \frac{K(\lambda-1)\mathcal{M}_-(\lambda,\theta)\mathcal{P}(\lambda)\cos 2\beta}{2\mu\mathcal{G}(\lambda,\theta)\mathcal{M}_-(\lambda,\beta)+2\mathcal{M}_-(\lambda,\theta)\mathcal{G}(\lambda,\beta)} + \frac{K\mathcal{M}_-(\lambda,\theta)\lambda[(\mu-\rho)(\lambda-2)-\mathcal{P}(\lambda)]}{2\mu\mathcal{G}(\lambda,\theta)\mathcal{M}_-(\lambda,\beta)+2\mathcal{M}_-(\lambda,\theta)\mathcal{G}(\lambda,\beta)}, \tag{A3}$$

$$D_l = -\frac{K\lambda\rho[2+\mathcal{H}_+(\lambda,\theta)]\mathcal{G}(\lambda,\beta)}{2\mu\mathcal{G}(\lambda,\theta)\mathcal{M}_-(\lambda,\beta)+2\mathcal{M}_-(\lambda,\theta)\mathcal{G}(\lambda,\beta)} + \frac{K\lambda\rho\mu\mathcal{M}_-(\lambda,\beta)\mathcal{M}_+(\lambda,\theta)}{2\mu\mathcal{G}(\lambda,\theta)\mathcal{M}_-(\lambda,\beta)+2\mathcal{M}_-(\lambda,\theta)\mathcal{G}(\lambda,\beta)} - \frac{K\mu\lambda(\lambda-1)(\lambda-2)\mathcal{H}_+(\lambda,\theta)(\cos 2\beta-1)}{2\mu\mathcal{G}(\lambda,\theta)\mathcal{M}_-(\lambda,\beta)+2\mathcal{M}_-(\lambda,\theta)\mathcal{G}(\lambda,\beta)}. \tag{A4}$$

The coefficients B_g, C_g and B_l, C_l can be easily expressed via obtained A_g, D_g and A_l, D_l:

$$C_g = -(K + A_g), \tag{A5}$$

$$C_l = -(K\rho + A_l), \tag{A6}$$

$$B_g = \frac{A_g[\cos\beta(\lambda-2)-\cos\beta\lambda]+K\cos\beta(\lambda-2)-D_g\sin\beta(\lambda-2)}{\sin\beta\lambda}, \tag{A7}$$

$$B_l = -\frac{A_g\cos\beta\lambda-(K+A_g)\cos\beta(\lambda-2)+D_g\sin\beta(\lambda-2)}{\sin\beta\lambda} + \frac{(\lambda-2)\big(D_g-D_l\big)}{\lambda}. \tag{A8}$$

[1] M. Singh, H. M. Haverinen, and P. Dhagat, Inkjet printing—Process and its applications, Adv. Mater. **22**, 673 (2010).
[2] J. Berthier, K. Brakke, E. Furlani, I. Karampelas, V. Poher, D. Gosselin, M. Cubizolles, and P. Pouteau, Whole blood spontaneous capillary flow in narrow V-groove microchannels, Sens. Actuators B: Chem. **206**, 258 (2015).
[3] E. Berthier, A. M. Dostie, U. N. Lee, J. Berthier, and A. B. Theberge, Open microfluidic capillary systems, Anal. Chem. **91**, 8739 (2019).
[4] A. Bender, P. Stephan, and T. Gambaryan-Roisman, A fully coupled numerical model for deposit formation from evaporating urea-water drops, Int. J. Heat Mass Transf. **159**, 120069 (2020).
[5] S. Kachel, Y. Zhou, P. Scharfer, C. Vrančić, W. Petrich, and W. Schabel, Evaporation from open microchannel grooves, Lab Chip **14**, 771 (2014).
[6] N. Kubochkin and T. Gambaryan-Roisman, Capillary-driven flow in corner geometries, Curr. Opin. Colloid Interface Sci. **59**, 101575 (2022).
[7] W. J. P. van Enckevort and J. H. Los, On the creeping of saturated salt solutions, Cryst. Growth Des. **13**, 1838 (2013).
[8] M. J. Qazi, H. Salim, C. A. W. Doorman, E. Jambon-Puillet, and N. Shahidzadeh, Salt creeping as a self-amplifying crystallization process, Sci. Adv. **5**, eaax1853 (2019).
[9] G. Liu, T. Chen, J. Xu, G. Yao, J. Xie, Y. Cheng, Z. Miao, and K. Wang, Salt-rejecting solar interfacial evaporation, Cell Rep. Phys. Sci. **2**, 100310 (2021).
[10] A.-M. Cazabat and G. Guéna, Evaporation of macroscopic sessile droplets, Soft Matter **6**, 2591 (2010).
[11] H. Y. Erbil, Evaporation of pure liquid sessile and spherical suspended drops: A review, Adv. Colloid Interface Sci. **170**, 67 (2012).
[12] R. G. Larson, Transport and deposition patterns in drying sessile droplets, AIChE J. **60**, 1538 (2014).
[13] D. Zang, S. Tarafdar, Y. Y. Tarasevich, M. D. Choudhury, and T. Dutta, Evaporation of a droplet: From physics to applications, Phys. Rep. **804**, 1 (2019).
[14] S. K. Wilson and H.-M. D'Ambrosio, Evaporation of sessile droplets, Annu. Rev. Fluid Mech. **55**, 481 (2023).
[15] V. S. Ajaev and O. A. Kabov, Heat and mass transfer near contact lines on heated surfaces, Int. J. Heat Mass Transf. **108**, 918 (2017).
[16] R. D. Deegan, O. Bakajin, T. F. Dupont, G. Huber, S. R. Nagel, and T. A. Witten, Capillary flow as the cause of ring stains from dried liquid drops, Nature (London) **389**, 827 (1997).
[17] Y. Y. Tarasevich, Simple analytical model of capillary flow in an evaporating sessile drop, Phys. Rev. E **71**, 027301 (2005).
[18] B. J. Fischer, Particle convection in an evaporating colloidal droplet, Langmuir **18**, 60 (2002).
[19] H. Hu and R. G. Larson, Analysis of the microfluid flow in an evaporating sessile droplet, Langmuir **21**, 3963 (2005).
[20] H. Hu and R. G. Larson, Analysis of the effects of Marangoni stresses on the microflow in an evaporating sessile droplet, Langmuir **21**, 3972 (2005).
[21] H. Hu and R. G. Larson, Marangoni effect reverses coffee-ring depositions, J. Phys. Chem. B **110**, 7090 (2006).
[22] W. D. Ristenpart, P. G. Kim, C. Domingues, J. Wan, and H. A. Stone, Influence of substrate conductivity on circulation reversal in evaporating drops, Phys. Rev. Lett. **99**, 234502 (2007).
[23] H. Bodiguel and J. Leng, Imaging the drying of a colloidal suspension, Soft Matter **6**, 5451 (2010).
[24] P. Stephan and C. Busse, Analysis of the heat transfer coefficient of grooved heat pipe evaporator walls, Int. J. Heat Mass Transf. **35**, 383 (1992).
[25] V. S. Ajaev, *Interfacial Fluid Mechanics: A Mathematical Modeling Approach* (Springer, New York, 2012).
[26] H. Han, C. Schlawitschek, N. Katyal, P. Stephan, T. Gambaryan-Roisman, F. Leroy, and F. Müller-Plathe, Solid–liquid interface thermal resistance affects the evaporation rate of droplets from a surface: A study of perfluorohexane on chromium using molecular dynamics and continuum theory, Langmuir **33**, 5336 (2017).

[27] J. W. Strutt, Steady motion in a corner of a viscous fluid, *Scientific Papers* (Cambridge University Press, Cambridge, 1920), Vol. 6, p. 18.
[28] W. R. Dean and P. E. Montagnon, On the steady motion of viscous liquid in a corner, Math. Proc. Cambridge Philos. Soc. **45**, 389 (1949).
[29] H. K. Moffatt, Viscous and resistive eddies near a sharp corner, J. Fluid Mech. **18**, 1 (1964).
[30] H. K. Moffatt, Some topological aspects of fluid dynamics, J. Fluid Mech. **914**, P1 (2021).
[31] O. Voinov, Extension of the problem of viscous fluid flow in a corner to the case of flow with curved boundaries, J. Appl. Math. Mech. **69**, 751 (2005).
[32] D. H. Michael and M. E. O'Neill, The separation of Stokes flows, J. Fluid Mech. **80**, 785 (1977).
[33] D. J. Jeffrey and J. D. Sherwood, Streamline patterns and eddies in low-Reynolds-number flow, J. Fluid Mech. **96**, 315 (1980).
[34] H. Gelderblom, O. Bloemen, and J. H. Snoeijer, Stokes flow near the contact line of an evaporating drop, J. Fluid Mech. **709**, 69 (2012).
[35] H. Gelderblom, H. A. Stone, and J. H. Snoeijer, Stokes flow in a drop evaporating from a liquid subphase, Phys. Fluids **25**, 102102 (2013).
[36] S. H. Hong, M. A. Fontelos, and H. J. Hwang, The contact line of an evaporating droplet over a solid wedge and the pinned–unpinned transition, J. Fluid Mech. **791**, 519 (2016).
[37] T. Okuzono, M. Kobayashi, and M. Doi, Final shape of a drying thin film, Phys. Rev. E **80**, 021603 (2009).
[38] H.-M. D'Ambrosio, T. Colosimo, B. R. Duffy, S. K. Wilson, L. Yang, C. D. Bain, and D. E. Walker, Evaporation of a thin droplet in a shallow well: Theory and experiment, J. Fluid Mech. **927**, A43 (2021).
[39] F. Carle, S. Semenov, M. Medale, and D. Brutin, Contribution of convective transport to evaporation of sessile droplets: Empirical model, Int. J. Therm. Sci. **101**, 35 (2016).
[40] V. S. Ajaev and O. A. Kabov, Evaporation and fluid flow near the boundary of a stationary dry patch, Phys. Rev. E **105**, 065111 (2022).
[41] N. A. Fuchs, *Evaporation and Droplet Growth in Gaseous Media* (Pergamon Press, New York, 1959).
[42] O. A. Kabov, D. V. Zaitsev, D. P. Kirichenko, and V. S. Ajaev, Interaction of levitating microdroplets with moist air flow in the contact line region, Nanoscale Microscale Thermophys. Eng. **21**, 60 (2017).
[43] M. S. A. Javed and V. S. Ajaev, Advection and deposition of microdroplets in stagnation point flow, Interfacial Phenom. Heat Transf. **11**, 103 (2023).
[44] D. Quéré, Wetting and roughness, Annu. Rev. Mater. Res. **38**, 71 (2008).
[45] P. T. Tsilingiris, Thermophysical and transport properties of humid air at temperature range between 0 and 100° C, Energy Convers. Manag. **49**, 1098 (2008).
[46] Y. O. Popov, Evaporative deposition patterns: Spatial dimensions of the deposit, Phys. Rev. E **71**, 036313 (2005).
[47] T. Gambaryan-Roisman, Simultaneous imbibition and evaporation of liquids on grooved substrates, Interfac. Phenom. Heat Transf. **7**, 239 (2019).
[48] A. Bilotti, Static temperature distribution in IC chips with isothermal heat sources, IEEE Trans. Electron Devices **21**, 217 (1974).